Numerical Prediction of Mean and Fluctuating Velocities for Jet-Flap Flows

A. J. Baker*
University of Tennessee, Knoxville, Tenn.
and
P. D. Manhardt†
Computational Mechanics Consultants, Inc., Knoxville, Tenn.

A method is developed to predict the flow characteristics in the near wake region of a jet over a finite chord wing surface of an upper surface blown flap. Transition distributions of mean flow and select fluctuating velocity correlations, within the region immediately downstream of a sharp-edged terminus of a slot nozzle-jet flap, are established using a parabolized form of the time-averaged steady flow Navier-Stokes equations closed with a turbulence kinetic energy model. Numerical solutions, obtained using a finite-element algorithm are presented which quantize the localized large mean flow accelerations and resultant peaks in the distribution of turbulence kinetic energy in the near wake region. Results are verified by comparison to experiment.

Nomenclature

a	= sound speed; boundary condition coefficient
C	= coefficient; wall porosity friction factor
e	= alternating tensor; finite-element index
f	= function of known argument
h	= slot nozzle height
H	= boundary-layer shape factor
I	= far-field acoustic intensity
k	= turbulence kinetic energy
K	= generalized diffusion coefficient
ℓ	= differential operator; turbulence length scale
L	= differential operator
M	= Mach number; number of finite elements spanning R
n	= unit normal vector
N	= finite-element cardinal basis function
p	= pressure; generalized parameter
P	= Stokes stress tensor
q	= generalized dependent variable
Q	= discretized generalized dependent variable
R	= domain of elliptic differential operator
Re	= Reynolds number
S	= acoustic source term; finite-element assembly operator
t	= time
T	= Lighthill stress tensor
u, U	= velocity
V	= scale velocity
x, y	= Cartesian coordinate system
∂R	= closure of solution domain R
δ	= Kronecker delta
ϵ	= turbulence dissipation function
λ	= scalar multiplier
μ	= dynamic viscosity
ν	= kinematic viscosity
ρ	= density

σ_{ij}	= mean flow Stokes stress tensor
τ_{ij}	= Reynolds stress tensor
Ω	= total solution domain

Subscripts

e	= finite-element domain
i, j, k, ℓ	= tensor indices
j	= jet reference condition
o	= initial condition
t	= turbulent
w	= reference condition at wall

Superscripts

e	= effective value
T	= matrix transpose
$(\tilde{\ })$	= mass-weighted time average
$(\bar{\ })$	= time average
$(\hat{\ })$	= unit vector
$(\ )'$	= mass-weighted fluctuating component; ordinary derivative
$(\ )^*$	= approximation

Boldface type is used to denote the nontensor index.

Introduction

TURBULENT boundary-layer flows departing an aerodynamic surface are experimentally verified to be strong sources of noise. Many investigators have experimentally measured far-field radiated noise associated with flow of a directed jet over an aerodynamic surface with trailing edge.[1-4] Interaction of the jet flow with the trailing edge has been established as an important noise source, with flap length relative to jet potential core length and jet velocity as correlation parameters. Alteration of the aerodynamic surface can change far-field intensity by local absorbtion as well as modifications of the turbulent flow structure before and after departing the trailing edge.[5,6]

The configuration of the aeroacoustic flowfield of general interest is shown in Fig. 1, illustrating a source of high-momentum fluid flowing over an aerodynamic surface. The flow leaves the surface at a sharp trailing edge, tangent to the mean chord in accordance with the Kutta condition, and proceeds to equilibration with the freestream. It is assumed that the flow is essentially unidirectional and parallel to the x_1 (curvilinear) coordinate as shown; hence $u_1 \gg u_2$, u_3 where u_i is the velocity vector.
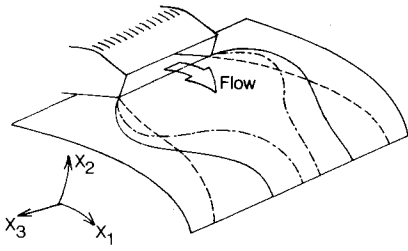
Fig. 1 Representative jet flow patterns over wing-flap surface, $M=0.8$[7]

The point of departure for an acoustic model is typically the theory of Lighthill.[8,9] Based upon first principles, the equation governing propagation of sound in a homogeneous medium at rest is

$$\frac{\partial^2 \rho}{\partial t^2} - a_0^2 \frac{\partial^2 \rho}{\partial x^2} = \frac{\partial^2 T_{ij}}{\partial x_i \partial x_j} \qquad (1)$$

where a_0 is the reference sound speed, and the solution domain is assumed devoid of solid surfaces. Equation (1) possesses the retarded-time solution

$$\rho - \rho_0 = \frac{1}{4\pi a_0^2} \frac{\partial^2}{\partial x_i \partial x_j} \int T_{ij}\left(y, t - \frac{|x-y|}{a_0}\right) \frac{dy}{|x-y|} \qquad (2)$$

The noise source mechanisms are described by the Lighthill stress tensor T_{ij}. A useful characterization is obtained by decomposition of the velocity field into mean time-averaged and fluctuating components as

$$u_i = \bar{u}_i + u_i' \qquad (3)$$

Applying the continuity equation, the source term in Eq. (1) in mean velocity field $\bar{u}_j$ is, employing a subscript comma for partial differentiation,

$$S \equiv \frac{\partial^2 T_{ij}}{\partial x_i \partial x_j} = \rho(\bar{u}_{j,i}\bar{u}_{i,j} + \bar{u}_{i,i}\bar{u}_{j,j}) - 2\bar{u}_i\rho_{,it} + \bar{u}_i\bar{u}_j\rho_{,ij}$$

$$+ 2\bar{u}_{i,j}(\rho u_j')_{,i} + 2(\bar{u}_{i,i}\rho u_j')_{,j} + (\rho u_i'u_j')_{,ij} + P_{ij,ji} - a_0^2\rho_{,jj} \qquad (4)$$

where P_{ij} is the mean flow Stokes stress tensor. The density derivative terms may be removed by a Galilean transformation. For small Mach number, temperature effects may also be neglected, which deletes the last two terms of Eq. (4). The source term that requires evaluation in a moving reference frame is then

$$S^* = \rho(\bar{u}_{j,i}\bar{u}_{i,j} + \bar{u}_{i,i}\bar{u}_{j,j}) + 2\bar{u}_{i,j}(\rho u_j')_{,i}$$

$$+ 2(\bar{u}_{i,i}\rho u_j')_{,j} + (\rho u_i'u_j')_{,ij} \qquad (5)$$

Analyses for elementary jet and wake flows typically idealize the mixing layer by assuming only $\bar{u}_1$ nonvanishing and independent of x_1. This removes the first and third terms in Eq. (5) and simplifies the remaining summations. However, for the jet-flap flow, the assumption that $\bar{u}_1 = \bar{u}_1(x_2)$ is inappropriate at the flap terminus where large local accelerations can occur. The shear layer assumption on transverse mean velocity remains valid, however, which yields the approximation

$$S^* \approx 2\bar{u}_{1,j}(\rho u_j')_{,1} + 2(\bar{u}_{1,1}\rho u_j')_{,j} + (\rho u_i'u_j')_{,ij} \qquad (6)$$

The third term in Eq. (6) was originally analyzed by Proudman[10] using an isotropic turbulence model for free jets. The lead term was first identified by Mollo-Christensen and Marasimbo.[11] In the terminology of Lilley,[12] the third term is

called the "self noise" due to its quadrupole nature. The first term is called the "shear noise" since the shear components are modified by the mean velocity derivative. The potential importance of the second term stems primarily from the existence of the terminus of the trailing edge.

Substituting Eq. (6) into Eq. (2), and utilizing a Galilean transformation, yields the solution expressed in a reference frame moving with the flow as

$$\rho - \rho_0 = \int \left[\frac{x_l}{2\pi a_0^3 M^2} \bar{u}_{l,j} \frac{\partial}{\partial t}(\rho u_j') + \frac{1}{2\pi a_0^2 M} \bar{u}_{l,lj}\rho u_j' \right.$$

$$\left. + \frac{x_j}{2\pi a_0^3 M^2} \bar{u}_{l,1} \frac{\partial}{\partial t}(\rho u_j') + \frac{x_i x_j}{4\pi a_0^4 M^3} \frac{\partial^2}{\partial t^2}(\rho u_i'u_j') \right] d\tau \qquad (7)$$

The far-field noise intensity is obtained from the variance of Eq. (7) in a fixed reference frame, as

$$I(x) \equiv (a_0^3/\rho_0)\overline{[\rho - \rho_0]_i[\rho - \rho_0]_j} \qquad (8)$$

The product is understood to include all possible tensor combinations. The overbar indicates time-averaged, and Eq. (8) represents the noise intensity measured at observer location x due to all coherent sources.

Evaluation of integrals in Eq. (8) is difficult, and modeling has been employed to express covariances in terms of correlations of the turbulent flowfield. For example, Eq. (8) becomes a single evaluation in a uniform mean flow with isotropic turbulence. Proudman,[10] using the concept of an eddy volume beyond which significant coherence vanishes, established the far-field intensity for a moving reference frame in terms of turbulence kinetic energy

$$k \equiv \frac{1}{2}\overline{u_i'u_i'} \qquad (9)$$

and isotropic turbulence dissipation function

$$\epsilon \delta_{ij} \equiv 3\bar{\nu} \overline{\frac{\partial u_i'}{\partial x_k} \frac{\partial u_j'}{\partial x_k}} \qquad (10)$$

Using the same procedure, Lilley[12] evaluated the far-field intensity due to the mean shear noise term, Eq. (6), in terms of k and a length scale ℓ_d, expressible in terms k and ϵ as

$$\ell_d \equiv k^{3/2}/\epsilon \qquad (11)$$

Moon and Zelazny[13] expanded the concept to an axisymmetric free jet, for which the shear term in Eq. (6) is nonvanishing for $j=2$, and additional terms result from the summation implied by the repeated subscripts in the self-noise term. Substitution of Eqs. (9-11) again yields Eq. (8), an explicit function of the distributions of turbulence correlations, which are now two dimensional, and the mean flow shear.

For the aerodynamic flow, over and downstream of the terminus of the flap, added complexity results from $\bar{u}_1$ becoming a function of both x_1 and x_2. Without swirl, $\bar{u}_2$ and $\bar{u}_3$ remain negligibly small to first order. Several additional terms may then assume importance in Eq. (6) as the j summations range over 1 and 2. Hence, both x_1 and x_2 derivatives of $\bar{u}_1$, as well as the turbulence correlations and several cross-product terms could result. For flaps with a sharp trailing edge and no flow separation, a parabolized form of the Navier-Stokes equations for steady time-averaged flow, coupled with a turbulence kinetic energy closure model, can describe the details of the flow structure. Simpler forms of these equations are routinely solved for attached boundary-layer flows[14] and for free shear layer mixing far removed from the source.[15] However, for the jet flap, the dominant action related to the noise generation appears to be the immediate wake vicinity of the trailing edge. An asymptotic

analysis of a simplified two-dimensional flow in this vicinity for laminar flow is reported[16] with extension to turbulent flow.[17]

An alternative approach reported herein is numerical solution of a parabolized form of the governing nonlinear differential equation system, including direct computation from the flap into the near wake. The parabolic Navier-Stokes equations for steady, time-averaged, two-dimensional flows are derived. The turbulence kinetic energy-dissipation function closure model is the minimum requirement, and the corresponding parabolic equation system is identified. A finite-element solution algorithm is established for the entire system, including all switching of boundary conditions and equation solution sequence. Numerical solutions are presented to document validity of the analysis procedure for cold-flow jets by comparison to experimental data.

Differential Equation System

The Navier-Stokes equation system becomes amenable to numerical solution techniques in a practical sense only after time-averaging. Employing the Reynold's decomposition, Eq. (3), where $\bar{u}_i$ is the mass-weighted, time-averaged velocity[18]

$$\bar{u}_i \equiv \overline{\rho u_i}/\bar{\rho} \tag{12}$$

and u_i' are the velocity fluctuations about the mean flow, the time-averaged Navier-Stokes equations for an isoenergetic flow are, in index notation,

$$L(\bar{\rho}) = \frac{\partial \bar{\rho}}{\partial t} + \frac{\partial}{\partial x_j}(\bar{\rho}\bar{u}_j) = 0 \tag{13}$$

$$L(\bar{\rho}\bar{u}_i) = \frac{\partial(\bar{\rho}\bar{u}_i)}{\partial t} + \frac{\partial}{\partial x_j}\left[\bar{\rho}\bar{u}_j\bar{u}_i + \frac{\partial \bar{p}}{\partial x_i} - (\bar{\sigma}_{ij} - \overline{\rho u_i'u_j'})\right] = 0 \tag{14}$$

In Eq. (14), $\bar{\sigma}_{ij}$ is the time-averaged Stoke's stress tensor,

$$\bar{\sigma}_{ij} \equiv \frac{\bar{\mu}}{Re}\left[\frac{\partial \bar{u}_i}{\partial x_j} + \frac{\partial \bar{u}_j}{\partial x_i} - \frac{2}{3}\frac{\partial \bar{u}_k}{\partial x_k}\delta_{ij}\right] \tag{15}$$

where $\bar{\mu}$ is the viscosity. The fourth term in the divergence is called the Reynolds stress tensor τ_{ij}:

$$\tau_{ij} \equiv -\overline{\rho u_i'u_j'} \tag{16}$$

A parabolic approximation to Eqs. (13-16) describes steady, confined or unbounded, viscous and turbulent flowfields wherein: 1) a predominant flow direction is uniformly discernible; 2) only in this direction are diffusion processes negligible compared to convection; and 3) no significant flowfield disturbances are propagated upstream in the flow. For the predominant flow direction assumed parallel to x_1, eliminating diffusion in this direction yields the parabolic form for Eq. (15) as

$$\bar{\sigma}_{ij} = \frac{\bar{\mu}(1-\delta_{il})}{Re}\left[\frac{\partial \bar{u}_i}{\partial x_j} + \frac{\partial \bar{u}_j}{\partial x_i} - \frac{2}{3}\frac{\partial \bar{u}_k}{\partial x_k}\delta_{ij}\right] \tag{17}$$

The bold face type denotes the index on δ_{il} not eligible for summation, but is simply synonymous with the identical tensor index.

The mean flow unidirectionality assumption affects terms retained in the Reynold's stress summation as well. An exact partial differential equation can be established for $-\overline{u_i'u_j'}$, the kinematic Reynolds stress.[18] The transport equation for isotropic turbulence dissipation function, Eq. (10), is also available.[19] These seven additional partial differential equations, describing turbulence phenomena, are not closed, however, since the third-order correlations remain undefined. Modeling of these correlations is typically invoked to close the

system. For example, Hanjalić and Launder[20] establish a closure applicable to thin shear flows wherein only $-\overline{u_1'u_2'}$ is retained, and solved in combination with ϵ and the turbulence kinetic energy k, Eqs. (9) and (10). For the unidirectional, shear-dominated flows of present interest, wherein $\bar{u}_1 \gg \bar{u}_2, \bar{u}_3$, the parabolic approximation to the Reynold's transport equations for k and ϵ are

$$L(k) = \frac{\partial}{\partial x_j}(\bar{u}_j k) - C_k \frac{\partial}{\partial x_\ell}\left[\frac{k^2}{\epsilon}\frac{\partial k}{\partial x_\ell}\right] - \overline{u_1'u_\ell'}\frac{\partial \bar{u}_1}{\partial x_\ell} + \epsilon = 0 \tag{18}$$

$$L(\epsilon) = \frac{\partial}{\partial x_j}(\bar{u}_j\epsilon) - C_\epsilon \frac{\partial}{\partial x_\ell}\left[\frac{k^2}{\epsilon}\frac{\partial \epsilon}{\partial x_\ell}\right]$$

$$- C_\epsilon'\overline{u_1'u_\ell'}\frac{\epsilon}{k}\frac{\partial \bar{u}_1}{\partial x_\ell} + C_\epsilon^2\frac{\epsilon^2}{k} = 0 \tag{19}$$

In Eqs. (18) and (19), the various constants C_α are determined from approximate analyses and/or computer optimization.[20,21] Furthermore, these equations define a summation index convention, appropriate for parabolic flows as, $1 \le i,j \le 3$ and $2 \le \ell \le 3$.

An additional simplification, employed for the present analysis, is specification of an effective turbulent diffusion coefficient ν_t. From first principles, the coefficient must be of the form

$$\nu_t \equiv V\ell \tag{20}$$

where V is a scale velocity and ℓ a scale length. For the turbulence kinetic energy-dissipation function two-equation closure hypothesis (TKE), V is taken as the square root of turbulence kinetic energy, and ℓ is the dissipation length scale ℓ_d, Eq. (11), yielding

$$\nu_t \equiv C_\nu k^2 \epsilon^{-1} \tag{21}$$

The parabolic mean flow equation system can now be closed, using Eq. (21) to model the correlation between the shear components of the Reynold's stress tensor and k and ϵ. Viewing Eq. (17), and neglecting dilitation, the relation is assumed of the form

$$-\overline{u_i'u_\ell'} \equiv C\nu_t\left[\frac{\partial \bar{u}_i}{\partial x_\ell} + \frac{\partial \bar{u}_\ell}{\partial x_i}\right] \tag{22}$$

using the defined parabolic index convention, and C is a scalar constant. An effective diffusion coefficient can then be written as

$$\mu^e \equiv (1/Re)\bar{\mu} + \bar{\rho}\nu_t \tag{23}$$

The parabolized partial differential equation system for the steady mean flow and turbulence closure, using the defined two-equation model and effective diffusion coefficient, then becomes

$$L(\bar{\rho}) = \frac{\partial}{\partial x_i}(\bar{\rho}\bar{u}_i) = 0 \tag{24}$$

$$L(\bar{u}_i) = \frac{\partial}{\partial x_j}(\bar{\rho}\bar{u}_j\bar{u}_i) - \frac{\partial}{\partial x_\ell}\left[\mu^e\left(\frac{\partial \bar{u}_i}{\partial x_\ell} + \frac{\partial \bar{u}_\ell}{\partial x_i}\right)\right] + \frac{\partial \bar{p}}{\partial x_i} = 0 \tag{25}$$

$$L(k) = \frac{\partial}{\partial x_j}(\bar{\rho}\bar{u}_j k) - \frac{\partial}{\partial x_\ell}\left[C_k\mu^e\frac{\partial k}{\partial x_\ell}\right] - \mu^e\frac{\partial \bar{u}_1}{\partial x_\ell}\frac{\partial \bar{u}_1}{\partial x_\ell} + \bar{\rho}\epsilon = 0 \tag{26}$$

$$L(\epsilon) = \frac{\partial}{\partial x_j}(\bar{\rho}\tilde{u}_j \epsilon) - \frac{\partial}{\partial x_\ell}\left[C_\epsilon \mu^e \frac{\partial \epsilon}{\partial x_\ell}\right]$$

$$- C'_\epsilon \frac{\epsilon}{k}\mu^e \frac{\partial \tilde{u}_l}{\partial x_\ell}\frac{\partial \tilde{u}_l}{\partial x_\ell} + C_\epsilon^2 \rho \frac{\epsilon^2}{k} = 0 \qquad (27)$$

where ν_t has been replaced everywhere by μ^e since $\bar{\rho}\nu_t \gg \bar{\mu}$. The tensor indices range $1 \le i,j \le 3$ and $2 \le \ell \le 3$ for three-dimensional flows, and $1 \le i,j \le 2$, $\ell = 2$ only for two-dimensional flows. Hence, since $i = 1$ corresponds to the direction of predominant flow, diffusion is restricted to the plane transverse to the x_l coordinate, as required by the parabolic assumption.

Equations (24-27) provide the general description of the parabolized Navier-Stokes equations. For ducted or exterior swirling flows, additional derivational steps are required to provide a parabolic closure model for pressure.[22] For the essentially planar nonswirling external flows to which this analysis is directed, an order-of-magnitude simplification can decouple the pressure field. Assuming the wake flow initialized by the merging of dissimilar turbulent boundary-layer profiles, without separation and at a sharp trailing edge, to second order from Eq. (25) for $i = 2$, the transverse pressure distribution through the individual profiles is balanced by a normal Reynolds stress component as

$$L[\bar{p}(x_2)] \approx \frac{\partial}{\partial x_2}\left[\bar{p} + \overline{\rho u'_2 u'_2}\right] = 0 \qquad (28)$$

The static pressure distribution for a planar slot nozzle-jet flap configuration is a constant, and only modestly variable in the wake of an elementary isolated airfoil. Hence, to first order, Eq. (28) describes the transverse pressure distribution in a planar shear layer wake behind a sharp trailing edge. Similarly, the axial pressure gradient in Eq. (25) for $i = 1$ is solely that induced by the inviscid potential flow, and $\partial \tilde{u}_l/\partial x_l$ is negligible compared to $\partial \tilde{u}_l/\partial x_\ell$. Expanding Eq. (25) for $i = 2$, using Eq. (28) and redefining terms using the continuity Eq. (24) and the turbulent viscosity closure model, Eqs. (22) and (23), the transverse mean flow momentum equation becomes

$$L(\tilde{u}_2) = \frac{\partial}{\partial x_j}(\bar{\rho}\tilde{u}_i\tilde{u}_j) - \frac{\partial}{\partial x_\ell}\left[\mu^e \frac{\partial \tilde{u}_2}{\partial x_\ell}\right] + e_{3ij}\frac{\partial \tilde{u}_l}{\partial x_j}\frac{\partial \mu^e}{\partial x_i} = 0 \quad (29)$$

and e_{3ij} is the Cartesian alternating tensor.

The essential differential character of the established equation system is initial value in the x_l coordinate and boundary value in the (x_2, x_3) plane. The starting solution plane, and the location of boundary condition specifications, are denoted in Fig. 2 for the basic two-dimensional planar slot nozzle-jet flap configuration. All variables vanish identically
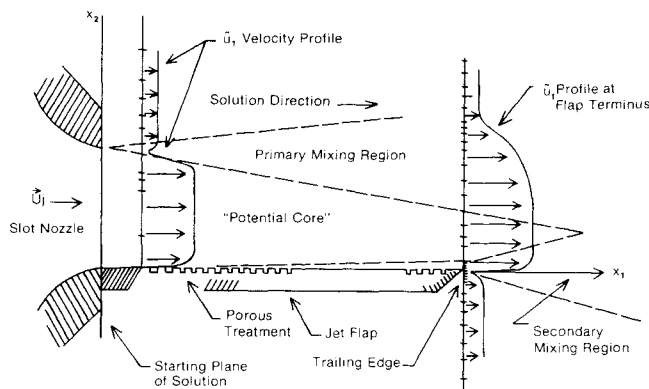

Fig. 2 Two-dimensional symmetry plane flowfield for rectangular slot nozzle-planar jet-flap configuration.

on the flap surface segment, except if it is assumed porous, whereupon $\tilde{u}_2$ takes on a specified nonzero value, i.e., $\tilde{u}_2 \equiv V_w$. For the planar flap symmetry plane cases studied, the freestream pressure is uniform; therefore, to first order, the freestream pressure gradient vanishes, and Eq. (28) provides the second-order estimate of pressure variation. The continuity Eq. (24) provides the freestream boundary condition for solution of Eq. (29) for transverse velocity in the secondary mixing region. For the boundary-layer solution on the flap surface, Eq. (24) is solved directly for $\tilde{u}_2$ as an initial-value problem in the x_2 coordinate direction. Hence, a complete jet-flap flowfield solution requires a switching of equation solution procedure as the flow departs the flap trailing edge.

Finite-Element Solution Algorithm

The parabolized partial differential equation system governing unidirectional aeroacoustic jet-flap flows has been developed. Each is a special case of a second-order, nonlinear elliptic boundary value problem

$$L(q) = \frac{\partial}{\partial x_\ell}\left[K\frac{\partial q}{\partial x_\ell}\right] + f_1\left(q, \frac{\partial q}{\partial x_k}, p, x_i\right) + f_2\left(\tilde{u}_l, \frac{\partial q}{\partial x_l}\right) = 0 \qquad (30)$$

In Eq. (30), q is the generalized dependent variable representing u_i, k, and ϵ, the tensor indices range $2 \le k, \ell \le 3$ and $1 \le i \le 3$, K is the effective diffusion coefficient, f_1 is a specified function of its argument, and f_2 is the initial-value operator. Boundary conditions for each variable are contained within

$$\ell(q) = a^1 q + a^2 K(\partial q/\partial x_\ell)n_\ell + a^3 = 0 \qquad (31)$$

i.e., the normal derivative of q is constrained by q and a parameter as determined by specification of the a^i. An initial condition is also required for q identified with each dependent variable as,

$$q(x_l^0, x_2, x_3) \equiv q_0(x_2, x_3) \qquad (32)$$

The finite-element solution algorithm is based upon the assumption that $L(q)$ for all q is uniformly parabolic within a bounded open domain Ω; that is, the lead term in Eq. (30) is uniformly elliptic within its domain R, with closure ∂R, where

$$\Omega \equiv R \times x_l \qquad (33)$$

and $x_l^0 \le x_l$. Equation (31) expresses functional constraints on the closure of Ω, $\partial\Omega \equiv \partial R \times x_l$, and the initial-condition specification, Eq. (32), lies on $R \cup \partial R \times x_l^0$.

The concept of the finite-element algorithm involves the assumption that each three-dimensional dependent variable is separable on $\Omega_e \equiv R_e \times x_l$, where R_e is the finite-element domain, in the form

$$q_e(x_l, x_\ell) = q_1(x_l)q_\ell(x_2, x_3) \qquad (34)$$

The functional dependence in $q_\ell(x_2, x_3)$ is represented by a polynomial in x_ℓ. The expansion coefficients q_1 can be conveniently expressed in terms of the values of $q_e(x_l, x_\ell)$ at the nodes of the finite-element discretization of R. Upon rearrangement, Eq. (35) then becomes

$$q_e(x_l, x_\ell) \equiv \{N(x_\ell)\}^T\{Q(x_l)\}_e \qquad (35)$$

where the polynomial set $N(x_\ell)$ are known functions of x_2 and x_3. Since they are known, they can be differentiated analytically, e.g.,

$$\frac{\partial q_e}{\partial x_2} = \frac{\partial}{\partial x_2}\left[\{N(x_\ell)\}^T\right]\{Q(x_l)\}_e \qquad (36)$$

Hence, there is never a need to use difference formulas to approximate the differentiated terms in $L(q)$ on R_e.

The finite-element solution algorithm is established for the equation system (30-32) using the method of weighted residuals (MWR) formulated on a local basis. Hence, the algorithm is valid for nonlinear equation systems, since there is no assumption of existence of an energy functional for minimization. The expansion coefficients in Eq. (35) are determined by requiring the local error in the approximate solution to both the differential equation $L(q_e)$ and the boundary condition statement $\ell(q_e)$, for $\partial R_e \cap \partial R$, be rendered orthogonal to the space of the interpolation functions $\{N(x_\ell)\}$. Employing an algebraic multiplier λ, the resultant equation sets are combined as

$$S_e \left[\int_{R_e} \{N(x_\ell)\} L(q_e) d\tau - \lambda \int_{\partial R_e \cap \partial R} \{N(x_\ell)\} \ell(q_e) d\sigma \right] \equiv \{0\}$$

(37)

where S_e is the operator mapping functions on the finite-element subspace R_e onto the global domain R, commonly termed the assembly operator. The number of Eqs. (37) prior to assembly is identical with the number of node points of the finite-element R_e.

Equation (37) forms the basic operation of the finite-element solution algorithm and of the computer program embodiment. The lead term can be rearranged, and λ determined, using a Green-Gauss theorem:

$$\int_{R_e} \{N(x_\ell)\} \frac{\partial}{\partial x_\ell} \left[K \frac{\partial q_e}{\partial x_\ell} \right] d\tau = \oint_{\partial R_e} \{N(x_\ell)\} K \frac{\partial q_e}{\partial x_\ell} \hat{n}_\ell d\sigma$$

$$- \int_{R_e} \frac{\partial}{\partial x_\ell} \{N(x_\ell)\} K \frac{\partial q_e}{\partial x_\ell} d\tau$$

(38)

For $\partial R_e \cap \partial R$ nonvanishing, the corresponding segment of the closed-surface integral will cancel the boundary condition contribution, Eq. (37) by identifying λa^2 unity, Eq. (30). The contributions to the closed-surface integral, Eq. (38) whereat $\partial R_e \cap \partial R = 0$ can also be made to vanish. The globally assembled finite-element solution algorithm for the representative partial differential equation system then becomes

$$S_e \left[- \int_{R_e} \frac{\partial}{\partial x_\ell} \{N\} K \frac{\partial q_e}{\partial x_\ell} d\tau + \int_{R_e} \{N\} (f_{1e} + f_{2e}) d\tau \right.$$

$$\left. - \int_{\partial R_e \cap \partial R} \{N\} (a^1 q_e + a^3) d\sigma \right] \equiv \{0\}$$

(39)

The rank of the global equation system (39) is identical with the total number of node points on $R \cup \partial R$ for which the dependent variable requires solution. Equation (39) is a first-order, ordinary differential system for all q. Solution of this system is obtained using a finite-difference numerical integration algorithm. The continuity Eq. (24), which is retained for the boundary-layer solutions, is also an ordinary differential equation, numerical integration of which yields the required solution at node points of the discretization.

Numerical Results

A numerical project was completed to establish nonuniform discretizations yielding acceptable solution accuracy for turbulent flows predicted using the derived finite-element solution algorithm. The standard two-dimensional boundary-layer equations are a subset of Eqs. (24-27), with Eq. (25) for $j = 2$ discarded and $\ell = 2$ only elsewhere. Equations (26) and (27) were solved for the turbulent kinetic energy closure model using Eq. (23) to evaluate effective viscosity. Comparison results were also established
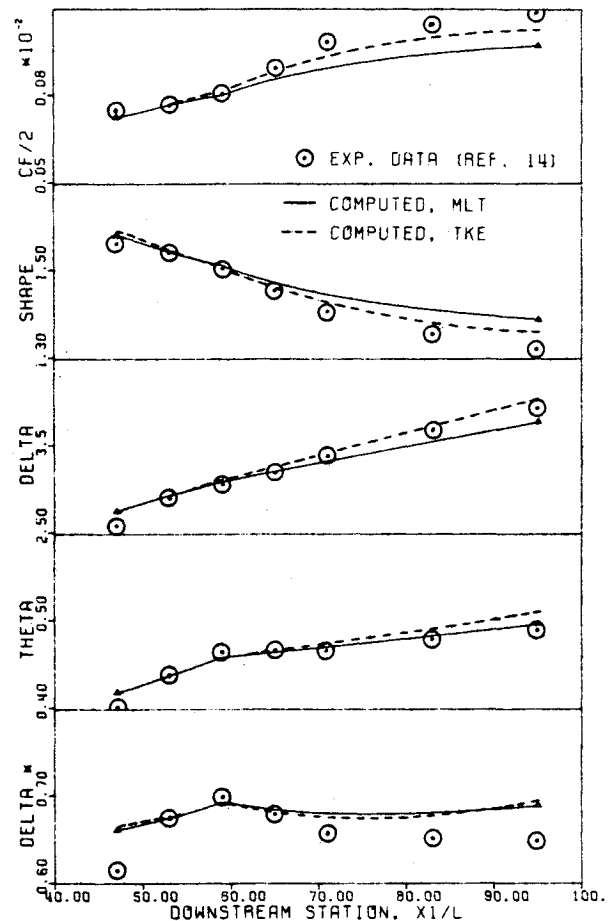

Fig. 3 Boundary-layer parameters, Bradshaw relaxing flow.

using mixing length theory (see Cebeci and Smith[18]) to provide closure, as well as to supply a sublayer turbulence model for initiation of the turbulent kinetic energy and dissipation profiles for the trailing-edge studies. Shown in Fig. 3 is a comparison of computed results to experimental data in terms of boundary-layer integral and point parameters for the Bradshaw nonequilibrium data set in Ref. 14. Agreement is generally good with minor differences exhibited between the closure models. Additional details on accuracy, convergence, and solution initiation are given in Ref. 23.

The parabolized Navier-Stokes equation system was evaluated for flow prediction accuracy for the basic slot nozzle-jet flap geometry illustrated in Fig. 2. Experimental configurations have typically employed rectangular slot nozzles to form the jet flow, with aspect ratios (slot width to height) in the vicinity of 50:1. Important three-dimensional effects are then limited to the extremum boundary regions, while the core flow approximates a two-dimensional character. Experimental data were taken by Schrecker and Maus[2] on the symmetry centerplane downstream of a slot nozzle-jet flap configuration of aspect ratio 60:1. This case was selected to evaluate predicted distributions of mean flow velocity and turbulence correlations.

The computational solution domains are illustrated in Fig. 4. The jet flow is accelerated by the nozzle to a nominal $U_j = 120$ m/s immediately downstream. The jet interacts with the freestream within the primary mixing region, and a turbulent boundary-layer flow develops adjacent to the flap which erodes the inviscid potential core at a rate difference from the free shear layer mixing in the primary region. The flap terminates at a sharp trailing edge. Immediately thereafter, a secondary mixing region is engendered between the jet boundary-layer flow and the entrained flow. The initially zero $\bar{u}_l$ on the flap surface is rapidly accelerated
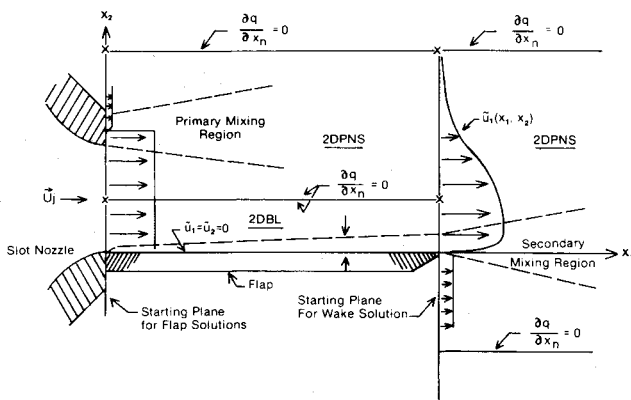
Fig. 4 Two-dimensional flowfield specifications for rectangular slot nozzle-planar jet-flap configuration.
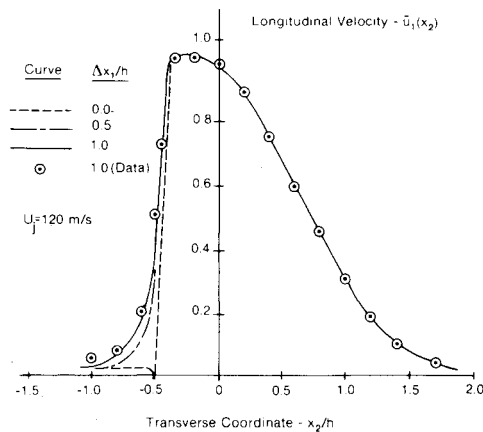

Fig. 6 Turbulent velocity profiles downstream of jet flap.

Fig. 5 Longitudinal velocity profiles downstream of jet flap.

Fig. 7 Computed wake distributions of mean axial velocity, turbulent kinetic energy, and effective viscosity.

within the immediate downstream vicinity of the flap terminus. The large x_2 gradient of $\bar{u}_1$ associated with the turbulent boundary layer is consequently dissipated, and acts in the process as a strong source term for generation of turbulence kinetic energy, see Eq. (26). Well downstream of the flap, the slot flow approaches a jet bounded by two free shear-layer mixing regions.

The computational simulation of this composite jet-flap flow was accomplished employing the two-dimensional boundary layer (2DBL) and parabolized (2DPNS) equation systems and the TKE closure model. Since no experimental data were available to initialize the solution, a uniform profile for $\bar{u}_1$ at the nozzle was assumed, and $\bar{u}_2$, k, and ϵ were started at zero levels. The lower jet flow developed on the flap as a boundary layer, completely isolated from the primary mixing region shear flow by the jet potential core. This was considered adequate, since experiment verified that the gradient-free potential core persisted well into the wake, and the far-field pressure was the constant associated with a free jet flow over a planar surface. The free shear-layer mixing within the primary region was initialized using a step profile in $\bar{u}_1$. The boundary-layer and primary mixing region solutions were marched downstream and matched together at the trailing edge, $x_1/h = 5.6$, where h is the slot nozzle height. A new solution domain was specified to encompass the two flows, plus the lower entrained flow, and a 2DPNS solution initialized to proceed into the wake region, see Fig. 4. The lower freestream $\bar{u}_1$ entrainment velocity was estimated from data and assumed laminar at the trailing edge. Boundary conditions for individual solutions within each domain are also noted in Fig. 4. Details on solution initiation are presented in Ref. 23.

Figure 5 presents comparison between computed $\bar{u}_1$ profiles, at select stations downstream of the trailing edge,
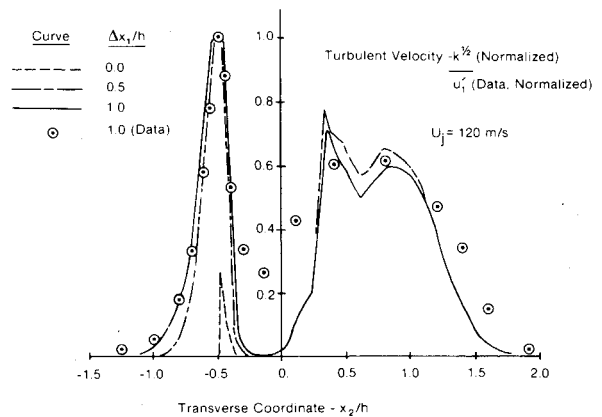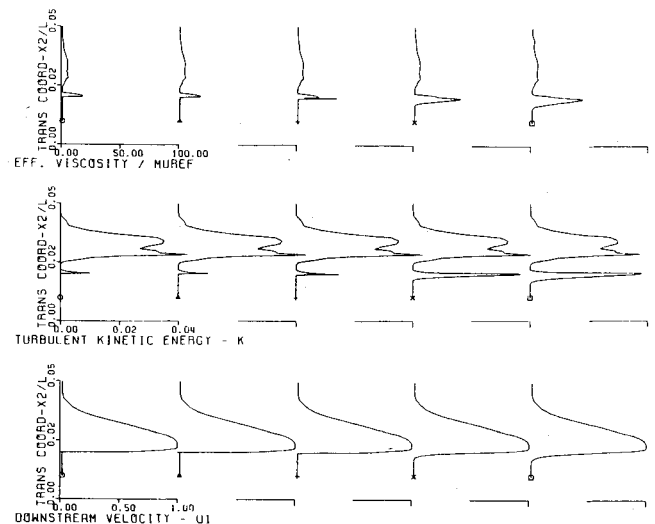
and experimental data at $x_1/h = 6.6$. Excellent agreement is indicated, with the largest differences existing in the profile wings where the jet merges with the entrained flow. Shown in Fig. 6 is the comparison of corresponding computed turbulence kinetic energy profiles to data on $-u_1'u_1'$ at $x_1/h = 6.6$. Excellent agreement exists in the secondary mixing region, but the computed k levels in the primary region only approximate the data in an average sense. The experimental data indicate nonzero levels of $-u_1'u_1'$ therein. The computed levels of k in the primary region are very sensitive to the local level of $\bar{u}_1$ and the assumed-constant local dissipation length scale. Hence, these differences are most probably associated with the initiation procedure for the primary mixing region flow, and an inadequate accounting of the blunt base flow region at the nozzle upper face, see Fig. 3.

For the secondary mixing region, the illustrated agreement with data confirms validity of the initiation procedure and the flowfield model using 2DPNS. The strong interaction immediately downstream of the flap terminus is of primary interest. The extremum mean flow gradients exist therein, both in the x_1 and x_2 coordinate directions, and the corresponding generation rate of turbulence is likely a maximum. Shown in Fig. 7 are axial mean velocity, turbulent kinetic energy, and effective viscosity profiles at select stations immediately downstream of the trailing edge. The initial zero $\bar{u}_1$ level on the flap rapidly accelerates yielding the typical shear-layer profile. Since the mean flow velocity gradient persists, turbulence kinetic energy is continuously generated downstream of the peak formation rate illustrated. The peak region broadens as the flow proceeds further

downstream, and the maximum level of k increases by an additional 25%. As a direct consequence, there results a pronounced overall increase in the level of turbulence within the flowfield due to the flap terminating. The peaked distribution in the primary mixing region is not dissipated, since the computed effective diffusion coefficient therein is very small, as illustrated.

Numerical evaluation of spatial derivatives of $\bar{u}_l$ and k in the wake region could be employed in a noise model derived from Eqs. (6-8). The peak x_l derivative of $\bar{u}_l$ immediately downstream of the flap terminus is of the order 10^7, and decreases to 10^4 one slot height downstream. The $\bar{u}_l$ derivatives in the x_2 direction would contribute to the shear noise term. Calculated extremal values of $\partial \bar{u}_l / \partial x_2$ in the immediate wake are the order 10^6 and decrease to 10^5 at one slot height downstream. For turbulent kinetic energy, the extremal x_l and x_2 derivatives are both of order 10^7 and persist well downstream of the trailing edge. If the noise model utilizes the eddy volume concept, a length scale can be extracted from the computed turbulence parameters, see Eq. (11). Extremum dissipation lengths of 0.0075 m and 0.0018 m correspond to the computed k and ϵ distributions, and compare favorably with the experimental longitudinal and transverse space autocorrelation by Tam and Reddy.[24]

Treatment of an acoustically "hard" flap surface in the form of surface porosity is experimentally verified to alter far-field acoustic intensity.[5,6] An aerodynamically acceptable procedure could employ a mechanically formed mesh surface through which mass flow could be induced by generation of modest pressure differentials. Attenuation of far-field sound power level may result partially from alteration of the local turbulent flowfield. A computational simulation is direct, since the equivalent boundary condition statement is a controlling mechanism of the numerical solution for the flowfield. The acoustic surface treatment is assumed correlated by an elementary form of Bernoulli's equation:

$$\Delta p = -C\rho_w V_w^2 \qquad (40)$$

where Δp is the pressure difference across the porous surface, $\rho_w V_w$ is the resultant induced colinear mass flux, and C is an experimental friction factor. The pressure difference exists between the exterior flow and a subsurface cavity, which may
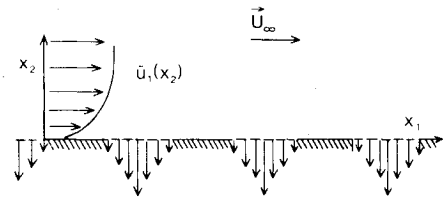
a)　Graph of porous surface mass flux periodicity, $V_{max} U_\infty^{-1} = 0.001$
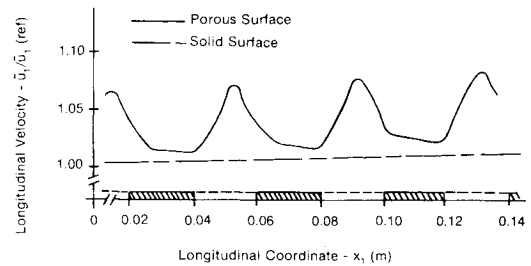
b)　Longitudinal velocity near porous surface $\bar{u}_l$

Fig. 8　Influence of porous surface treatment on turbulent flow.

possess a family of acoustic waves traveling at the characteristic cavity frequencies. Hence, one expects that Δp is a distributed function of x_l; dependent upon the cited factors, the induced V_w may be of variable sign and magnitude. Figure 8 illustrates a two-dimensional simulation of a periodic porosity influence on the $\bar{u}_l$ velocity component adjacent to a surface. A modest efflux accelerates the local mean flow by up to about 10%, with a corresponding increase in $\partial \bar{u}_l / \partial x_2$. The period equals that of the applied pressure wave with a lag of about one-quarter of the period.

The two-dimensional hard flap configuration of Schrecker and Maus[2] was altered to simulate a continuous distribution of surface porosity. The wave form approximates a sine with amplitude $V_w / U_\infty = \pm 0.03$ and period $\Delta x_l / h = 0.04$, where h is the slot-nozzle height. In the downstream flap region, $5.0 \leq x_l / h \leq 5.6$, the standard case boundary-layer flow was approaching fully turbulent with a shape factor $H = 1.6$. This flow was rerun with the cited porosity distribution to determine the extremum induced modifications to H and the computed $\bar{u}_l$ directly above the flap surface. The results are summarized in Table 1. A 2DPNS solution in the trailing-edge wake then assessed the influence of these porosity-induced flowfield modifications upon evolution within the secondary mixing region. Table 2 summarizes the results in terms of longitudinal mean velocity and turbulence kinetic energy at two levels above the flap (x_2 / h) and at several downstream stations. Turbulence mixing within the immediate secondary mixing region appears quite sensitive to the detailed structure of the turbulent boundary-layer flow at the flap terminus.

Table 1　Porosity-induced jet-flap flowfield modifications

Case no.	Description	Velocity Transverse, V_w / U_j	Velocity Longitudinal, $\bar{u}_l / U_j$	Shape factor, H
1	Standard (hard)	0	0.092	1.63
2	Influx (soft)	+0.03	0.031	1.87
3	Efflux (soft)	−0.03	0.148	1.57

Table 2　Select mean flow and turbulence velocities within the initial secondary mixing region as a function of simulated flap surface porosity

Coordinates, x_i / h Downstream $(i=1)$	Coordinates, x_i / h Vertical $(i=2)$	Mean flow velocity, $\bar{u}_l / U_j$ Influx, case 2	Mean flow velocity, $\bar{u}_l / U_j$ Standard, case 1	Mean flow velocity, $\bar{u}_l / U_j$ Efflux, case 3	Turbulence kinetic energy, k/U_j^2 Influx, case 2	Turbulence kinetic energy, k/U_j^2 Standard, case 1	Turbulence kinetic energy, k/U_j^2 Efflux, case 3
5.6	0.0014	0.031	0.094	0.148	10^{-6}	10^{-6}	10^{-6}
	0.0	0.0	0.0	0.0	0.0	0.0	0.0
5.601	0.0014	0.042	0.081	0.133	0.0006	0.0013	0.0063
	0.0	0.032	0.050	0.09	0.0005	0.0020	0.0044
5.65	0.0014	...	0.344	...	...	0.0358	...
	0.0	...	0.320	...	...	0.0368	...
5.76	0.0014	0.336	0.378	0.362	0.0300	0.0451	0.0376
	0.0	0.327	0.370	0.355	0.0300	0.0436	0.0374
5.92	0.0014	0.389	0.414	0.378	0.0331	0.0431	0.0382
	0.0	0.384	0.408	0.373	0.0335	0.0431	0.0382

Conclusions

A simplified parabolic form of the Navier-Stokes equations for the description of aeroacoustic flows over the basic jet-blown flap configuration has been established. A finite-element numerical formalism is employed to cast the identified initial-boundary value equation systems for steady, time-averaged turbulent flows into equivalent systems of ordinary differential equations. Computed evolution of the turbulent flow on the symmetry centerplane of a rectangular slot-nozzle-planar jet-flap geometry, and downstream of the sharp-edged terminus of the flap, compared favorably with experimental data. The influence of a porous treatment of the flap surface on the detailed flow structure on and downstream of the flap terminus was evaluated.

The results generally confirm the validity of the suggested approach to characterization of turbulent flows departing the sharp trailing edge of a planar flap. The developed concepts should be equally applicable to nonplanar geometries by extension of the theory for pressure coupling.

Acknowledgment

References

[1] Gruschka, H. D. and Schrecker, G. O., "Aeroacoustic Characteristics of Jet Flap Type Exhausts," AIAA Paper 72-130, 1972.

[2] Schrecker, G. O. and Maus, J. R., "Noise Characteristics of Jet-Flap Type Exhaust Flows," NASA CR-2342, 1974.

[3] Paterson, R. W. and Amiet, R. K., "Isolated Airfoil-Tip Vortex Interaction Noise," Journal of Aircraft, Vol. 12, Jan. 1975, pp. 34-40.

[4] Filler, L., "Prediction of Far-Field Jet/Trailing-Edge Interaction Noise for Engine Over-The-Wing Installations," AIAA Paper 76-518, 1976.

[5] Hayden, R. E., Kadman, Y., and Chanaud, R. C., "A Study of the Variable Impedance Surface Concept as a Means for Reducing Noise from Jet Interaction with Developed Lift-Augmenting Flaps," NASA CR-112166, 1972.

[6] Hayden, R. E., "Exploratory Investigation of Aeroacoustic Optimization of the Variable Impedance Edge Concept Applied to Upper Surface Blown Configurations," NASA CR-2714, 1976.

[7] Von Glahn, U. and Groesbeck, D., "Nozzle and Wing Geometry Effects on OTW Aerodynamic Characteristics," AIAA Paper 76-622, 1976.

[8] Lighthill, M. J., "On Sound Generated Aerodynamically, I," Proceedings of the Royal Society, A211, 1952, pp. 564-587.

[9] Lighthill, M. J., "On Sound Generated Aerodynamically, II," Proceedings of the Royal Society, A222, 1954, pp. 1-32.

[10] Proudman, I., "The Generation of Noise by Isotropic Turbulence," Proceedings of the Royal Society, A214, 1953, pp. 119-132.

[11] Mollo-Christensen, E. and Marasimbo, R., "Sound Emission from Jets at High Subsonic Velocities," Journal of Fluid Mechanics, Vol. 8, Pt. 1, 1960, pp. 49-60.

[12] Lilley, G. M., "On Noise from Air Jets," ARC, Vol. 20, 1958.

[13] Moon, L. F. and Zelazny, S. W., "Experimental and Analytical Study of Jet Noise Modeling," AIAA Journal, Vol. 13, March 1975, pp. 387-393.

[14] Proceedings, AFOSR-IFP-Stanford Conference on Computation of Turbulent Boundary Layers, Vol. 1, edited by S. J. Kline, G. Sovran, M. V. Morkovan, and D. J. Cockrell, 1968; Vol. II, edited by D. A. Coles and E. A. Hirst, Thermosciences Div., Dept. Mechanical Engineering, Stanford Univ., 1969.

[15] "Free Turbulent Shear Flows," NASA SP-321, July 1972.

[16] Melnik, R. E. and Chow, R., "Asymptotic Theory of Two-Dimensional Trailing-Edge Flows," NASA SP-347, 1975, pp. 177-249.

[17] Melnik, R. E. and Chow, R., "Turbulent Interaction at Trailing Edges," NASA CP-2001, 1976, pp. 1423-1424.

[18] Cebeci, T. and Smith, A. M. O., Analysis of Turbulent Boundary Layers, Academic Press, New York, 1974.

[19] Tennekes, H. and Lumley, J. L., A First Course in Turbulence, The MIT Press, Cambridge, Mass., 1974.

[20] Hanjalic, K. and Launder, B. E., "A Reynolds Stress Model of Turbulence and its Application to Thin Shear Flows," Journal of Fluid Mechanics, Vol. 52, Pt. 4 1972, pp. 609-638.

[21] Launder, B. E., Reece, G. J., and Rodi, W., "Progress in the Development of a Reynolds-Stress Turbulence Closure," Journal of Fluid Mechanics, Vol. 68, Pt. 3, 1975, pp. 537-566.

[22] Baker, A. J. and Manhardt, P. D., "An Interaction Solution Algorithm for Viscous Aerodynamic Performance Prediction," AIAA Paper 78-153, 1978.

[23] Baker, A. J. and Manhardt, P. D., "Finite Element Analysis of Aeroacoustic Jet-Flap Flows," NASA CR-2931, 1977.

[24] Tam, C. K. W. and Reddy, N. N., "Sound Generated in the Vicinity of the Trailing Edge of Upper Surface Blown Flap," AIAA Paper 76-503, 1976.